Distinctive role of ocean advection anomalies in the development of the extreme 2015–16 El Niño

Esteban Abellán · Shayne McGregor ·

Matthew H. England · Agus Santoso

Abstract The recent 2015–16 El Niño was of comparable magnitude to the two previous record-breaking events in 1997–98 and 1982–83. To better understand how this event became an extreme event, we examine the underlying processes leading up to the peak of the event in comparison to those occurring in the 1997–

E. Abellán

ARC Centre of Excellence for Climate System Science, and Climate Change Research Centre, University of New South Wales, Sydney, New South Wales, Australia

E-mail: esteban.abellan@unsw.edu.au

S. McGregor

School of Earth, Atmosphere and Environment, Monash University, Clayton, Victoria, Australia

Matthew H. England

ARC Centre of Excellence for Climate System Science, and Climate Change Research Centre, University of New South Wales, Sydney, New South Wales, Australia

Agus Santoso

ARC Centre of Excellence for Climate System Science, and Climate Change Research Centre, University of New South Wales, Sydney, New South Wales, Australia

98 and 1982–83 events. Differences in zonal wind stress anomalies are found to be
an important factor. In particular, the persistent location of the zonal wind stress
anomalies north of the equator during the two years prior to the 2015–16 peak
contrasts the more symmetric pattern and shorter duration observed during the
other two events. By using linear equatorially trapped wave theory, we determine
the effect of these off-equatorial westerly winds on the amplitude of the forced
oceanic Rossby and Kelvin wave response. We find a stronger upwelling projection
onto the asymmetric Rossby wave during the 2-yr period prior to the peak of the
most recent event compared to the two previous events, which might explain the
long-lasting onset. Here we also examine the ocean advective heat fluxes in the
surface mixed layer throughout the event development phase. We demonstrate
that, although zonal advection becomes the main contributor to the heat budget
across the three events, meridional and vertical advective fluxes are significantly
larger in the most recent event compared to those in 1997–98 and 1982–83. We
further highlight the key role of advective processes during 2014 in enhancing the
sea surface temperature anomalies, which led to the big El Niño in the following
year.

Keywords extreme El Niño · westerly wind anomalies · Kelvin and Rossby wave
projections · ocean currents · meridional asymmetry

1 Introduction

The El Niño-Southern Oscillation (ENSO) is the most dominant mode of interan-
nual climate variability; characterized by warming (El Niño) or cooling (La Niña)
of the tropical central and eastern Pacific sea surface, and associated large-scale

changes in sea level pressure, winds and convection (e.g., Rasmusson and Arkin 1985). The three strongest El Niño events ever observed - the 1982–83, 1997–98 and most recent 2015–16 event - all exhibited exceptional warming across the central-eastern equatorial Pacific (e.g. L'Heureux et al 2016) (Fig. 1). This warming pushed the edge of the western Pacific warm-pool eastward, and as a consequence atmospheric convection also shifted from the western equatorial Pacific to the usually cold and dry equatorial central-eastern Pacific (Cai et al 2014). Although all ENSO events, regardless of strength, can affect climate over many regions of the world (e.g. Philander 1990), the strongest El Niño events have been associated with the most significant natural disasters and socio-economic impact (Cai et al 2014). Thus, it is of crucial importance to better understand the mechanisms controlling the evolution and intensity of these strong El Niño events.

It is well known that El Niño events are generally preceded by and coincide with anomalous westerly winds, which are considered a requirement to release the available energy stored in the anomalous warm water volume (WWV) (Kessler 2002; Philander and Fedorov 2003; Zavala-Garay et al 2004; McGregor et al 2016; Levine and McPhaden 2016). Westerly wind bursts (WWBs) preceding El Niño events have been shown to play an important role triggering El Niño events (Latif et al 1988; Lengaigne et al 2004), whereas the buildup of the WWV in the equatorial Pacific is considered a necessary precondition for the development of an El Niño (Wyrtki 1985; Meinen and McPhaden 2000; An and Kang 2001). The occurrence of strong WWBs in early 2014 (Menkes et al 2014; Chen et al 2015) led many seasonal forecast teams to warn of a possible El Niño event by the end of the year, while the coincident near record Pacific WWV anomalies in March led many experts to warn that the anticipated event may rival the catastrophic

1997–98 event (Ludescher et al 2014; Tollefson 2014). However, the anticipated event never eventuated, as surface ocean warming ceased following the absence of westerly wind events from April to July 2014 (Menkes et al 2014), signifying a lack of air-sea coupling (McPhaden 2015).

Recent studies by Hu and Fedorov (2016, 2017), and Levine and McPhaden (2016) have suggested that the easterly wind bursts that occurred in the boreal summer were responsible for halting the development of this event, with relatively dry atmospheric conditions despite higher than normal sea surface temperature (SST). Furthermore, after an initial Ekman induced discharge of WWV (McGregor et al 2016), these easterlies would ultimately recharge equatorial heat content some months later (Jin 1997), priming the system for the 2015 El Niño (Levine and McPhaden 2016). Another recent study (Imada et al 2016) suggested the subsurface cool anomalies in the South Pacific Ocean as one of the reasons for the failed materialization of an El Niño in 2014. During the first few months of 2015 a new episode of strong westerly wind bursts combined with an abundance of WWV, allowing El Niño conditions to rapidly re-intensify (McPhaden 2015) (Fig. 2).

The spatial patterns of SST anomalies around the peak of the strong El Niño events in 2015–16, 1997–98 and 1982–83 are comparable in magnitude along the central equatorial Pacific (Fig. 1 shading and Fig. 2) being 2.6±0.1, 2.4±0.1 and 2.3±0.2°C, respectively, in the Niño-3.4 region averaged during November-January (NDJ). Despite similar central Pacific event magnitudes, weaker warming off the west coast of South America is evident during 2015–16. Further, as pointed out by L'Heureux et al (2016) and Xue and Kumar (2017), the 2015–16 SST anomalies in the western tropical Pacific were warmer. The evolution of SST anomalies (Fig.

2a) is clearly different across the three events, with values at the beginning of

the El Niño years across the three events, being $0.58\pm0.04^{\circ}$C in January 2015,

$-0.46\pm0.05^{\circ}$C in January 1997 and $0.16\pm0.08^{\circ}$C in January 1982. Consistent with

the weaker SST anomalies in the far eastern equatorial Pacific in the most recent

event, the SSH anomalies also exhibit weaker values than the other two events.

The aim of this study is to investigate the physical mechanisms that controlled

the development of the extreme El Niño event of 2015–16, and how they differed

from the past two strongest El Niño events observed since the satellite era began

in 1979. To this end, we first describe the datasets and analyses methods used in

Sect. 2. In Sect. 3, we analyze zonal wind stress and sea surface height anomalies

during the months prior to the peak of these strongest observed El Niño events.

Based on both the results presented in Sect. 3 and the key role for ocean advec-

tion in generating ENSO SST anomalies along the equator in central and eastern

equatorial Pacific (Wang and McPhaden 2000; Vialard et al 2001), we examine

the associated ocean advective fluxes during the events in Sect. 4. In Sect. 5 we

compare the two-year warming phenomenon of 2014–2015–2016 with the 1986–

1987–1988 event, which did not become a super El Niño. Finally, the main results

are summarized and discussed in Sect. 6.

2 Datasets and methodology

2.1 Datasets

This study employs the National Centers for Environmental Prediction (NCEP)

Global Ocean Data Assimilation System (GODAS; Behringer et al (1998); Behringer

and Xue (2004)), the European Centre for Medium-Range Weather Forecasts

107 (ECMWF) Ocean Re-Analysis system 4 (ORA-S4; Balmaseda et al (2013)) and

108 the Predictive Ocean Atmosphere Model for Australia (POAMA) Ensemble Ocean

109 Data Assimilation System (PEODAS; Yin et al (2011)) to compute the advection

110 terms in the heat budget equation in addition to the heating rate term. Multiple

111 products were utilised here to validate the heat budget analysis, as suggested by

112 Su et al (2010), and provide a measure of the robustness of any results presented.

113 The models have horizontal resolutions of $1\,^{\circ} \times 0.3\,^{\circ}$, $1\,^{\circ} \times 1\,^{\circ}$ and $2\,^{\circ} \times 0.5\,^{\circ}$, and

114 vertical resolutions within the mixed layer (upper 50m) of 10m, 10m, and 15m,

115 respectively. For the upper ocean heat content calculation, defined as depth aver-

116 aged temperature in the upper 300m, the last vertical levels of GODAS dataset

117 (shown in Fig. 2 are 205, 215, 225, 238, 262 and 303m. For all variables, anomalies

118 are calculated by removing the long-term monthly climatology over the period

119 1980–2015. As there is no direct output of the vertical velocity field in ORA-S4,

120 this variable is calculated from the horizontal currents by using the continuity

121 equation.

122   The SST datasets used here are the Hadley Centre Sea Ice and Sea Surface

123 Temperature dataset version 1 (HadISST1; Rayner et al (2003)), the Extended

124 Reconstructed Sea Surface Temperature version 3 (ERSSTv3; Smith et al (2008)),

125 the Centennial in situ Observation-Based Estimates of SST (COBE; Ishii et al

126 (2005)) and the Interim ECMWF Re-Analysis (ERA-Interim; Dee et al (2011)).

127 These reanalysis have a resolution of $1\,^{\circ} \times 1\,^{\circ}$, $2\,^{\circ} \times 2\,^{\circ}$, $1\,^{\circ} \times 1\,^{\circ}$ and $0.75\,^{\circ} \times$

128 $0.75\,^{\circ}$, respectively. Wind stress data are from the NCEP-National Center for At-

129 mospheric Research (NCEP-NCAR) Reanalysis 1 (NCEP1; Kalnay et al (1996)),

130 PEODAS (Yin et al 2011) and ERA-Interim (Dee et al 2011) with resolutions of

131 $2.5\,^{\circ} \times 2.5\,^{\circ}$, $2\,^{\circ} \times 0.5\,^{\circ}$ and $1.5\,^{\circ} \times 1.5\,^{\circ}$, respectively. We note here that the

surface wind products selected for analysis are largely consistent with those used

to force the ocean reanalysis data sets examined (GODAS and NCEP1, PEODAS

with PEODAS and ORA-S4 with ERA-Interim). Surface wind stress data was

only available for PEODAS dataset, which is made up of ERA-40 (Uppala et al

2005) prior to 2002 and NCEP Reanalysis II (Kanamitsu et al 2002) thereafter.

For the other two datasets the surface winds were converted to wind stresses us-

ing the quadratic stress law (Wyrtki and Meyers 1976): $(\tau_x, \tau_y) = C_D \rho_a W(U, V)$

where U and V are the zonal and meridional surface winds (m s^{-1}) respectively;

W denotes the surface wind speed (m s^{-1}), $C_D = 1.5 \times 10^{-3}$ is the dimensionless

drag coefficient; and $\rho_a = 1.2$ kg m^{-3} represents the atmospheric density at the

surface.

The SSH fields used in this study are from GODAS (Behringer et al 1998;

Behringer and Xue 2004), PEODAS (Yin et al 2011), ORA-S4 (Balmaseda et al

2013), whose resolutions are the same as for the heat budget variables, and the ob-

served Archiving, Validation, and Interpretation of Satellite Oceanographic (AVISO),

with $0.25\,^\circ \times 0.25\,^\circ$ of spatial resolution and daily temporal resolution. Global

mean sea level rise was removed by subtracting each month's global mean from

each SSH for each product. As for the heat budget computation, the anomalous

values of the rest of the variables are computed as the deviation of the 1980–2015

climatology.

Ideally, reanalysis with shorter timescales than a month might lead to resolve

non-linear processes, such as vertical mixing or those arising from tropical insta-

bility waves. Hence, our heat content results must be viewed with this caveat in

mind. However, we emphasize that in order to validate the heat budget analysis,

156 as suggested by Su et al (2010), multiple ocean assimilation data products have

157 been used in this study.

158 2.2 Methodology

159 *2.2.1 Kelvin-Rossby wave projections*

160 To examine the effect of the westerly wind anomalies on the amplitude of the

161 forced oceanic Rossby and Kelvin weave response, we use linear shallow water

162 wave theory described in McGregor et al (2016). The linear first baroclinic mode

163 shallow water equations can produce observed variations of ocean heat content,

164 sea surface heights (e.g., McGregor et al 2012a,b) and Niño-3 and Niño-3.4 indexes

165 (Abellán and McGregor 2016) reasonably well when the model is forced by wind

166 stress anomalies.

167   It is shown that the Hermite functions provide the meridional structure of

168 the oceanic Rossby and Kelvin wave response to the wind stress forcing (Clarke

169 2008). Using observed anomalous wind stresses as model forcing, we solve for the

170 amplitude of the forced oceanic Rossby and Kelvin waves using the method of

171 characteristics (e.g., Clarke 2008; McGregor et al 2016). A gravity wave speed (c)

172 of 2.8 m s^{-1} is used, which is consistent with observational estimates (Chelton

173 et al 2000), where Kelvin waves propagate eastward with a speed of c, while the

174 nth order Rossby waves propagate westward with a speed of $-c/(2n + 1)$.

175   As the only eastward propagating waves available in this model are Kelvin

176 waves, conservation of mass and the longwave approximation dictate that Rossby

177 wave mass transport at the western boundary must be balanced by the Kelvin

178 wave mass transport (e.g., Kessler 1991).

2.2.2 Ocean heat advection analaysis

We consider the total mixed layer heat balance can be expressed as follows (e.g.

Qiu 2000; Qu 2003; Du et al 2005; Santoso et al 2010; Cai et al 2015):

$$\frac{\partial T}{\partial t} = \frac{Q_{net}}{\rho_o c_p h} - u\frac{\partial T}{\partial x} - v\frac{\partial T}{\partial y} - w\frac{\partial T}{\partial z} + Res \qquad (1)$$

where T denotes the mixed layer temperature, which is a good proxy for SST,

Q_{net} represents the net surface heat flux, ρ_a is the reference oceanic density (1026

kg m^{-3}), c_p is the specific heat capacity of seawater (3986 J kg^{-1} K^{-1}), h is the

depth of the mixed layer, and $-\mathbf{u}\cdot\nabla T$ denotes the advective fluxes. The fifth

term on the right-hand side of Eq. (1) *Res* indicates all remaining unresolved

processes, including lateral diffusion, vertical mixing, and the shortwave radiation

that escapes through the base of the mixed layer (Paulson and Simpson 1977;

Santoso et al 2010). This residual term also includes any unresolved processes that

are not captured over the monthly time-scales of interest in this study, such as the

impact of tropical instability waves. Although the focus of this work is instead

on the monthly-evolving ocean advection terms in the heat budget equation (Eq.

1), an estimate of residual term along with the surface air-sea heat flux term is

included in Sect. 6. The mixed layer depth is assumed to be constant in our study

and is taken to be 50 m as in several past studies (e.g. An and Jin 2004; Thual

et al 2011; Imada and Kimoto 2012; Hua and Yu 2015). This is motivated by the

Cane and Zebiak model for ENSO (Zebiak and Cane 1987), which has been shown

to give a reasonable representation of the mixed layer depth in the central Pacific

(de Boyer Montégut et al 2004; Lorbacher et al 2006).

The total oceanic advection of heat can be decomposed as:

$$\mathbf{u} \cdot \nabla T = \bar{u}T'_x + u'\bar{T}_x + u'T'_x + \bar{v}T'_y + v'\bar{T}_y + v'T'_y + \bar{w}T'_z + w'\bar{T}_z + w'T'_z \quad (2)$$

where u, v, w represent the zonal, meridional and vertical ocean current velocities, overbar denotes the monthly mean climatology, prime denotes the anomaly (relative to the monthly climatology) and the subscript denotes the partial derivative in that particular direction.

The use of multiple reanalysis products allows us to assess the statistical significance of reanalysis mean differences in the heat budget advection terms between the 2015–16 event and the 1982–83 and 1997–98 events. In order to achieve this, we use a two-sample *Student* t-test to assess the significance of mean differences, in which the significance is determined at the 95% confidence level.

3 Evolution of zonal wind stress and sea surface height anomalies

3.1 Zonal wind stress anomalies

The anomalous westerly winds that precede El Niño events, as mentioned before, can be made up of higher frequency (intra-seasonal) bursts and a lower frequency and large-scale Bjerkness feedback component, a combination of which can be seen in the monthly latitude-time sections of the zonal wind stress (Fig. 3). Here, the 2015–16 event anomalous winds appear to be distinct from the earlier events in several other ways. As reported by L'Heureux et al (2016), the 2015–16 event equatorial winds were weaker than those of the 1997–98 event. For instance, the zonal wind averaged between 5°S-5°N during the 12 months prior to the peak of the events are 0.68±0.24 and 1.23±0.02 $\times$ 10^{-2} N m^{-2}, respectively. Secondly,

the wind anomalies in the 2015–16 event display much more asymmetry about the

equator than the other two events, with the 2015–16 event primarily displaying

westerly (easterly) anomalies north (south) of the equator. This characteristic can

be also seen by the average values during the 12-month and 24-month periods

in Fig. 4, where the maximum anomalies occur at $5°N$ in the 2015–16 event and

only easterlies are found in the Southern Hemisphere, in contrast to the other two

events in which westerlies are found in both hemispheres. To better illustrate these

results, we consider an asymmetry index defined as the zonal wind in the Northern

Hemisphere $(0°\text{-}20°N)$ minus the Southern Hemisphere $(20°S\text{-}0°)$ averaged over

both, the 12-month and 24-month periods prior to the event peak. The 3 reanalysis

product average indices for each event (Table 1) highlight the strong meridional

asymmetry of the 2015–16 event (three times larger than that in the 1997–98

event), while statistical tests suggest that this difference is statistically significant.

Note the significance test is conducted by comparing the index of the 2015–16 event

from each reanalysis product against the indices from all three reanalysis products

for both the 1997–98 and 1982–83 events. We find that the main difference is in

the Southern Hemisphere (Table 1), with easterly anomalous wind in the 2015–

16 event and westerly (as in the Northern Hemisphere) in the other two events.

This persistent maximum westerly wind anomaly location north of the equator

is at least partly associated with highly unusual cyclone activity in the western

Pacific (Boucharel et al 2016a,b; Collins et al 2015). This unusual cyclone activity

has also been related to the substantially warmer SST anomalies over the north

tropical Pacific $(5°N\text{-}20°N)$ observed over the 2-yr period in the 2015–16 event

$(0.42\pm0.05°C)$ relative to 1997–98 $(0.07\pm0.02°C)$ and 1982–83 $(-0.06\pm0.03°C)$

(Fig. 5) (Murakami et al 2017).

Another prominent feature revealed by Fig. 3 is that for the 2015–16 event, anomalous westerly winds persisted as far back as the beginning of 2014. This is distinct from the 1997–98 and 1982–83 events, which had the largest anomalous westerly winds only beginning some 12 months prior to the peak of the events. This difference in wind persistence could indicate the role of the 2014–15 "failed event" in contributing to the emergence of the 2015–16 El Niño. As such, our analysis below in distinguishing the dynamics of these events will consider the genesis of the events over both the 12 and 24-month periods prior to the peak of the events, indicating the monthly temporal evolution and the average over these two periods. Furthermore, the warming conditions over the central equatorial Pacific in early 2015 (Fig. 2a) suggest that the previous year should be taken into account as a possible explanation of the large event.

To further understand the ocean response to the relaxation of the easterly trade winds during the onset of El Niño events, we calculate the first baroclinic mode projection coefficients for the eastward propagating Kelvin wave and the first four westward propagating trapped Rossby waves following the methodology detailed in McGregor et al (2016). As defined by the Hermite functions solutions to the shallow-water model equations, Rossby waves with odd (even) numbers produce thermocline anomalies that are symmetric (asymmetric) structure about the equa- tor (Kessler 1991; Fedorov and Brown 2009). The mode number also highlights several other key features of the Rossby waves, i) the higher the mode number, the slower and further away from the equator the main thermocline depth pertur- bation propagates; ii) even number Rossby waves do not generate an equatorial Kelvin wave upon impinging on the western boundary, and iii) the magnitude of the reflected Kelvin wave decreases as the odd order mode number increases

(Kessler 1991). The excitation of strong downwelling Kelvin waves observed since March 1997 and August 1982 until the peak of the related events (Fig. 6b-c), as a result of strong westerly wind anomalies (e.g., McPhaden 1999), contribute to the exceptional strength of El Niño events during 1997–98 and 1982–83, respectively. However, the 2015–16 El Niño event exhibits basinwide average projection coefficients that are up to four times much weaker than those of the preceding events (Fig. 6a, Table 2).

The first baroclinic mode $n = 1$ Rossby wave for the 2015–16 event also displays significantly weaker magnitudes during most of the 24-month period (Fig. 6d-f, Table 2). Interestingly, the downwelling Kelvin wave in March-April 2014 (Fig. 6a) had only a weak upwelling $n = 1$ Rossby wave signal in the far western Pacific (Fig. 6d), but also coincides with a strong central Pacific projection onto upwelling $n = 2$ and $n = 4$ Rossby waves (Fig. 6g, m) (i.e, both of which have no western boundary reflection), which might explain why the warming that started in 2014 was able to continue into 2015. Finally, the significantly stronger projection through much of the two years onto the asymmetric $n = 2$ and $n = 4$ Rossby waves in addition to the smaller Kelvin wave projection during the 2015–16 El Niño compared to the previous events (Fig. 6m-o, Table 2) are consistent with the asymmetric location of the westerly winds described above. We note that these two Rossby waves have weak impact of equatorial heat content (e.g., McGregor et al 2016), while the weaker Kelvin wave projection, which has a strong impact on equatorial heat content (McGregor et al 2016), indicates a weaker equatorial region WWV signal.

3.2 Sea surface height anomalies

The basin-wide average SSH anomalies (Fig. 7) exhibit significantly (above the 95 % level) larger negative values along the north off-equatorial region (5-15°N) throughout the 2-yr period in the 2015–16 event compared to the 1997–98 and 1982–83 events (Table 3). The strong basin-wide average SSH anomalies along the north off-equatorial region (Fig. 4c-d) are consistent with the basinwide projection onto Rossby waves, as the 2015–16 event displays a significantly stronger negative projection onto the asymmetric n = 4 Rossby waves observed over the entire two year period (Fig. 6e and Table 2).

Another striking feature of the basin-wide average SSH anomalies in the equatorial region is that the 2015–16 El Niño displays positive values between 5°S-5°N that persist throughout the whole 24-month period prior to the event peak. Although no statistically significant difference is found between the 24-month average of the 2015–16 El Niño and the other two events (Table 3), the earlier events exhibit positive anomalies largely during the 12-month period only that are more symmetrically distributed about the equator (Fig. 7). Again, the apparent 2-yr persistence of the equatorial positive SSH signal in the 2015–16 event and the larger upwelling in the northern region mentioned above point to the different hemispheric forcing conditions from the past events. This result is in good agreement with the findings of Di Lorenzo and Mantua (2016), who reported that the development of the 2015–16 event was influenced by the emergence of ocean heatwave in the North Pacific associated with the North Pacific Oscillation, which was widely referred to as "The Blob" in the media.

4 Ocean advective heat fluxes

Previous studies (Wang and McPhaden 2000, 2001; Vialard et al 2001; Huang et al 2010) have shown the influence of ocean advection during the onset of El Niño events. To further reveal the distinction among the events arising from the processes described in Sect. 3, we expect to see some differences in the advective constituents shown in Eq. (2) that lead to the growth of SST anomalies over the Niño-3.4 region ($170°$W – $120°$W and $5°$S – $5°$N) - a region which is used for ENSO operational forecast. We first examine the impact of both persistence and meridional asymmetry of westerly wind anomalies on the horizontal ocean currents anomalies (u' and v'). Figure 8 shows the time series of anomalous zonal and meridional ocean currents during the two years prior to the peak of the events averaged over the Niño-3.4 region. The zonal component of the 2015–16 El Niño event displays two clear eastward propagation periods in early 2014 and late 2014 as a consequence of westerly wind anomalies (Fig. 3a-c). These anomalous winds generate a zonal pressure gradient between the eastern and western tropical Pacific, which generates a meridional SSH gradient, being positive (negative) south (north) of the equator (Fig. 7), producing this eastward geostrophic current anomaly. The meridional asymmetry in the anomalous zonal winds seen in the 2015–16 El Niño event leads to a south-flowing ocean flow during the whole period prior to the event peak (Fig. 8b). This is a discernible difference compared to the 1997–98 and 1982–83 El Niño events, in which the meridional ocean current is near climatological values in 1996 and 1981, respectively.

We now explore how these dramatic differences of ocean currents between the most recent El Niño and the other two events described above influence the

magnitude of the events. Monthly anomalies of each individual advection term of the heat budget equation (Eq. 2) during the 24-month period prior to the peak of the events over the Niño-3.4 region are shown in Fig. 9. As expected from the time series of Niño-3.4 index (Fig. 2a), the warming tendency in the 1997–98 and 1982–83 El Niño events occurs mainly during the 12 months before the maximum amplitude of the events (Fig. 9a). While the major heating during the 2015–16 El Niño event also occurs during this period, it is interesting to note two periods of warming tendency in 2014, consistent with the 2014–15 failed event. There is a marked similarity between this total heating time evolution (Fig. 9a) and the zonal advection of climatological temperature by anomalous current ($u'\bar{T}_x$, Fig. 9c), suggesting the important role of this term in El Niño development (Huang et al 2010).

Here we aim to identify the dominant processes controlling the trajectory toward anomalous warming by integrating the advection terms over 24 and 12 months (i.e., expressed in degree Celsius) leading up to the peak of each event, respectively referred to "year -1" and "year 0". This approach allows a gauge of the relevance of the 2014 conditions for the development of the 2015–16 El Niño.

Figure 10 shows that the advective terms overall contribution to the total heating rate during all three strong El Niño events. Note that Q_{net} and the Res terms not shown constitute cooling rates, as mentioned before. Integrated over both 12 months and 24 months, the anomalous heating of all events is most strongly attributed to $u'\bar{T}_x$, followed by $\bar{v}T'_y$ and to a lesser extent by $\bar{w}T'_z$ (terms 3, 5, and 8). These terms respectively refer to the zonal advection of climatological temperature by anomalous currents, the meridional advection of anomalous temperature by mean currents, and the vertical advection of anomalous temperature by mean

upwelling. However, we note that, for the 1982–83 event, the heating contribution of $u'\bar{T}_x$ becomes small when integrated over the 24-month period, even displaying a weak damping effect in the GODAS reanalysis (Fig. 10d). This is mainly due to the fact that this term tended to cool SST during 1981 (Fig. 9c).

The total heating rate ($\partial T/\partial t$) integrated over 12 months prior to the peak of the 2015–16 event ($2.0\pm0.1^\circ$C) is significantly weaker than that for the 1997–98 and 1982–83 events ($3.0\pm0.4^\circ$C) (Fig. 10a). However, when integrated over 2 years, the heating rate for the 2015–16 event increases and becomes more comparable to the other two events in which the 1997–98 event shows a slight increase and the 1982–83 event a decrease (Fig. 10b). As demonstrated below, this reflects the importance of the 2014 ocean advection for the large magnitude of the 2015–16 El Niño. Focusing on the individual advection terms, there are no significant differences in the 12-month analysis between the 2015–16 event and past events, except for $u'\bar{T}_x$ when comparing the recent event to the 1997–98 event only. However, significant differences are found over the 24-month period in the $\bar{v}T'_y$, $v'\bar{T}_y$ and $\bar{w}T'_z$ terms, when comparing the 2015–16 event with the average of 1982–83 and 1997–98 events. The larger magnitude of $\bar{v}T'_y$, $v'\bar{T}_y$ and $\bar{w}T'_z$ indicate that these terms played a more prominent role in the growth of the 2015 El Niño with a notable contribution from the previous year. In particular, the sum of all advective terms contributes to much larger warming in the 2015–16 event ($9.2\pm1.5^\circ$C) compared to the other two events ($3.0\pm2.1^\circ$C).

It is worth emphasizing the large spread across the datasets in some terms of the heat budget analysis carried out in this study. For instance, the heating contribution of the main term ($u'\bar{T}_x$) varies between $2.1\,^\circ$C in ORA-S4 and $4.8\,^\circ$C in GODAS when integrated for the 24-month period in the 2015–16 event (Fig.

10d, f). Such a large spread is represented as a long error bar in Fig. 10b. To further examine the source of this big uncertainty, we decompose the advective terms into the single terms (i.e., velocities and gradients of temperature) for the two periods considered and annual mean climatological values (Fig. 11). The anomalous zonal current (u') for the 24-month period range between 0.07 and 0.15 m s^{-1} across the reanalysis products, being the minimum value around 50% less than the maximum value. However, the zonal climatological gradient of temperature ($\bar{T}_x$) for the same period is in the range -5.33×10^{-7} to -4.91×10^{-7} °C m^{-1}, which in this case is approximately 10% of difference between these two extreme values. We note that although the temperature gradients display uncertainties, they appear to be less important than the anomalous and climatological currents. In particular, the vertical velocity field exhibits the largest spread, with different sign for the 1982–83 event in both periods considered. It is noteworthy that in spite of the large spread across the three reanalysis products, the heat budget analyses derived from each product exhibit similar behaviour for the $\bar{v}T'_y$, $v'\bar{T}_y$ and $\bar{w}T'_z$ terms (Fig. 10c-h).

To further reveal the relative role of $\bar{v}T'_y$, $v'\bar{T}_y$ and $\bar{w}T'_z$ terms in the temporal evolution of the 2015–16 El Niño event (Fig. 2a), we now examine the temperature anomaly in the Niño-3.4 region integrated over the mixed layer that would occur if only the total advective terms were considered. This is done by integrating the variables forward in time starting from either January of year 0 (Fig. 12a) or January of year -1 (Fig. 12b), taking into account that the anomalous terms referred to the 2015–16 event (three members, one for each dataset) are computed as deviations from the 1997–98 and 1982–83 composite (six members). Comparing the anomalous three terms whose mean differences between the 2015–16 event and the other two events are significant ($\bar{v}T'_y$, $v'\bar{T}_y$ and $\bar{w}T'_z$), we find a positive

contribution throughout the entire 2-yr period. However, $u'\bar{T}_x$ (orange line), which

is a major heating term, particularly for the 2015–16 and 1997–98 events, leads

to warming during year -1 and cooling during year 0. The cooling effect of this

anomalous term is more evident when the integration starts instead in year 0 of

the event (i.e. only the 12-month lead-in window), showing smaller values than

what occurs for the 1997–98 and 1982–83 average. The anomalous all advective

terms combined (red line) exhibit the major heating during year -1 whereas the

increase in temperature is more gradual during year 0. Hence, the heating due to

advection terms during the last event is not considered distinct when compared to

past events over the 12-month period but it is distinct over the 24-month lead-in

period.

5 The 1987–88 El Niño

It is well known that one of the robust features of ENSO events is their tendency

to peak near the end of the calendar year (e.g. Rasmusson and Carpenter 1982).

However, the 1987–88 El Niño event evolved differently from the El Niño com-

posite, where a second peak occurred in September 1987 after the first peak in

January of the same year, which is the most common season (Fig. 2a). In view

of the unique two-year warming phenomenon of 2014–2015–2016, we also conduct

an additional analysis of the 1986–1987–1988 event examining the upper ocean

heat content (T300) as a proxy for the warm water volume and the heat budget

analysis.

The 2015–16 event displays a gradual increase of warm water volume, although

with some fluctuations, during the two years prior to the peak. However, the 1987–

88 event shows a dramatic fall after the first peak in early 1987 (Fig. 2b). This is

consistent with the findings by Zhang and Endoh (1994) in which they found that

the El Niño conditions in the eastern Pacific disappear in mid-1987 because of the

increase in trade winds over this region, whereas warm conditions remain in the

central and western Pacific until early 1988. To further elucidate why the 1987–88

event was not as strong as the 2015–16 event, we derive a heat budget for the Niño-

3.4 region during these two events (Fig. 13). We find that the zonal and meridional

advection of climatological temperature by anomalous currents terms ($u'\bar{T}_x$ and

$v'\bar{T}_y$) have opposite sign among these two events regardless the time period before

their peaks. For instance, the first term is equal to $-0.5\pm2.3\,^\circ$C for the 1987–88

event and $3.2\pm1.2\,^\circ$C for the 2015–16 event. This difference in the first term might

be related to the fact that there is a significant cooling in mid-1987 over the central

Pacific (Fig. 2a) in response to strong westward surface zonal advection (Zhang

and Endoh 1994). The much weaker meridional asymmetry in the westerly wind

anomalies for the 1987–88 event (with asymmetry index $= -0.38\pm0.08 \times 10^{-2}$ N

m^{-2} averaged over the 24-month period) leads to a poor contribution of $v'\bar{T}_y$ to

the development of this event in contrast to the 2015–16 El Niño event.

6 Summary and conclusions

Aiming to explain the mechanisms responsible for the strong 2015–16 El Niño, we

analyzed some climate variables such as SST, SSH and zonal wind stress during the

months prior to the peak and compared with the patterns seen in the two strong

events observed since 1979: the 1997–98 and 1982–83 events. While the magnitude

of SST and SSH anomalies over the central equatorial Pacific are comparable across

the 3 events, we found some obvious differences in the zonal wind stress anomalies that we now summarize below.

We found that the westerly wind stress anomalies are located either side of the equator in the previous extreme El Niño events, in contrast to the 2015–16 event, where anomalous winds are largely confined to the northern region of the tropical Pacific location. Another distinct feature of the most recent event is the early occurrence of these winds in the previous year (year -1), i.e., in early 2014, compared to the other two events in which they tend to concentrate in year 0 of the El Niño event.

Following McGregor et al (2016), we solved the amplitude of the forced oceanic Rossby and Kelvin wave response by specifying the temporal and spatial structure of the observed wind stress (Clarke 2008). We suggested that the downwelling Kelvin wave in April 2014, which had nearly no upwelling $n = 1$ Rossby wave signal but strong upwelling projection onto the $n = 2$ Rossby wave, without western boundary reflection, might explain the long-lasting warming initiated in 2014 and continued during 2015. We further related both the stronger projection onto the $n = 4$ Rossby wave and the smaller downwelling Kelvin wave projection to the meridional asymmetry of the anomalous westerly winds.

Motivated by these results, we carried out an analysis of the heat budget evolution of the surface mixed layer during the 24 months leading up to the event peak by examining its time evolution and its average over two periods: 12-month and 24-month periods prior to the event peak. We found that the development of the recent event, in terms of the rate of change of SST, during the 12-month period prior to the peak is weaker than that for the other events. However, when the 24-month period is considered as the growing phase, then all three events show

comparable values. Thus, this characteristic highlights that the physical processes occurring in 2014 play a key role in the large magnitude of the 2015–16 event that leads to warmer SST anomalies at the beginning of 2015 unlike near climatological values in early 1997 and 1982. This larger heat content during the pre-onset year of the most recent event is consistent with previous results reported by Menkes et al (2014).

One of the similarities among the three events analyzed here is that the anomalous heating is mostly attributed to $u'\bar{T}_x$, followed by $\bar{v}T'_y$ and to a lesser extent by $\bar{w}T'_z$. However, we found three advective fluxes with significant differences between the 2015–16 event and past strong events ($\bar{v}T'_y$, $v'\bar{T}_y$ and $\bar{w}T'_z$) whose link with the physical processes described in Sect. 3 can be summarized as follows: (1) the long-lasting and equatorial asymmetry of zonal wind anomalies in the 2015–16 event produce a larger $v'\bar{T}_y$ compared to the other events attributed to the lack of equatorward current south of the equator; (2) these two distinct features of zonal wind are at least partly related to the warmer SST anomalies north of the equator (e.g. Murakami et al 2017), which increase the importance of the $\bar{v}T'_y$; (3) finally, warmer ocean temperature anomalies underneath the mixed layer over the central equatorial Pacific (Fig. 14) would explain the larger values of $\bar{w}T'_z$ term ("Zhang and Gao 2017). We suggest that the driver of this warmer subsurface temperature, supported by higher WWV (Fig. 2b), during the most recent event might be related to deeper basin-wide average thermocline depth due to the long duration of westerly wind anomalies through the 2-yr period. Interestingly, the contribution of $u'\bar{T}_x$, which is related to the thermocline depth variations and zonal SSH gradients by geostrophic balance, during the 1-yr period for the 2015–16 event is much weaker than that for the 1997–98 event. This result supports the findings

presented recently by Paek et al (2017), where they reported that the thermocline anomalies during the 2015–16 event are much weaker than those during the 1997–98 event, suggesting a stronger influence of Central Pacific El Niño dynamics on the 2015–16 event than on the 1997–98 event. In line with this, the smaller Kelvin wave projection that we found would suggest that the thermocline feedback would not be as large during the most recent event.

Due to both the lack of data for the surface air-sea heat flux term Q_{net} in ORA-S4 and the unresolved processes included in the residual term, we have opted to retain focus on the role of the advective terms in the heat budget as these can be independently verified via an analysis of surface winds and sea surface height. However, for completion, we also present the time evolution of temperature budget anomalies of the strong El Niño events in the Niño-3.4 region for these two terms along with their contribution to the heat budget equation. Figure 15 reveals that the damping effect of these two terms in the most recent event was much larger than that in the two previous events, although this is significant for the residual term only. Thus, the stronger warming contribution to the total heat content of the advection terms during the 2015–16 El Niño event compared to the two previous events is consistent with the stronger cooling contribution of the total air-sea heat flux and the residual terms. The cooling effect of these two terms during the development year of El Niño events is consistent with previous studies (e.g. (Wang and McPhaden 1999, 2001; Huang et al 2010; Su et al 2010) in addition to the shortwave damping (Dommenget and Yu 2016). The large residual term could also be due to the fact that heat, freshwater, and momentum are not conserved in the ocean reanalysis systems and the weaker tropical instability waves activity during those years (Moum et al 2013).

Our conclusions are reached by examining three different ocean reanalysis products, which show largely consistent behavior albeit considerable spread across products. Thus, our results must still be viewed with some degree of caution in light of uncertainty in the reanalysis products as well as the assumption of a constant mixed layer depth in the Niño-3.4 region. It should be noted that we expect more uncertainty from the reanalysis products compared to this assumption. By way of example, the difference in the magnitude of advective terms averaged over the nine terms and 24-month period for the 2015–16 El Niño event between mixed layer depth assumption of $h = 30$ m and $h = 50$ m is 0.18 °C, whereas the difference across the products for $h = 50$ m is 0.26 °C. Finally, here we emphasized that although strong El Niño events have some robust features, such as the tendency for their peak to occur during boreal winter, every event has a somewhat different character. In this regard, we have demonstrated that ocean advection plays a key role during the growth of strong El Niño events. We further contrasted the 2015–16 event with the 1987–88 event; both events were preceded by warm equatorial Pacific in the previous year but the 1987–88 event failed to peak as a strong event due to the weak ocean advection.

Our results reaffirm the need for adequate ocean observations are required to more fully constrain reanalysis products and to better understand the mechanisms that control these variations across El Niño events, and in particular what makes these events grow in magnitude. This will ultimately help improve predictive skill for these significant and damaging climatic events.

References

Abellán E, McGregor S (2016) The role of the southward wind shift in both, the seasonal synchronization and duration of enso events. Clim Dyn 47:509–527

An SI, Jin FF (2004) Nonlinearity and Asymmetry of ENSO. J Climate 17(12):2399–2412

An SI, Kang IS (2001) Tropical Pacific basin-wide adjustment and oceanic waves. Geophys Res Lett 28:3975–3978

Balmaseda MA, Mogensen K, Weaver AT (2013) Evaluation of the ECMWF ocean reanalysis system ORAS4. Quart J Roy Meteor Soc 139:1132–1161

Behringer DW, Xue Y (2004) Evaluation of the global ocean data assimilation system at ncep. In: Eighth symposium on integrated observing and assimilation system for atmosphere, ocean, and land surface, AMS 84th annual meeting, Washington State Convention and Trade Center, Seattle, pp 11–15

Behringer DW, Ji M, Leetmaa A (1998) An improved coupled model for ENSO prediction and implications for ocean initialization. Part I: The ocean data assimilation system. Mon Wea Rev 126:1013–1021

Boucharel J, Jin FF, England MH, Dewitte B, Lin I, Huang HC, Balmaseda MA (2016a) Influence of oceanic intraseasonal Kelvin waves on the Eastern Pacific hurricane activity. J Climate 29:7941–7955

Boucharel J, Jin FF, England MH, Lin II (2016b) Modes of hurricane activity variability in the eastern Pacific: Implications for the 2016 season. Geophys Res Lett 43:11,358–11,366

de Boyer Montégut C, Madec G, Fischer AS, Lazar A, Iudicone D (2004) Mixed layer depth over the global ocean: An examination of profile data and a profile-

based climatology. J Geophys Res Oceans 109:C12,003

Cai W, Borlace S, Lengaigne M, van Rensch P, Collins M, Vecchi G, Timmermann A, Santoso A, McPhaden MJ, Wu L, England MH, Wang G, Guilyardi E, Jin FF (2014) Increasing frequency of extreme El Niño events due to greenhouse warming. Nature Clim Change 4:111–116

Cai W, Wang G, Santoso A, McPhaden MJ, Wu L, Jin FF, Timmermann A, Collins M, Vecchi G, Lengaigne M, England MH, Dommenget D, Takahashi K, Guilyardi E (2015) Increased frequency of extreme La Niña events under greenhouse warming. Nature Clim Change 5:132–137

Chelton DB, Wentz FJ, Gentemann CL, de Szoeke RA, Schlax MG (2000) Satellite microwave SST observations of transequatorial tropical instability waves. Geophys Res Lett 27:1239–1242

Chen D, Lian T, Fu C, Cane MA, Tang Y, Murtugudde R, Song X, Wu Q, Zhou L (2015) Strong influence of westerly wind bursts on El Niño diversity. Nature Geosci 8:339–345

Clarke A (2008) An introduction to the dynamics of El Niño and the Southern Oscillation, vol ISBN: 9780120885480. Academic Press

Collins JM, Klotzbach PJ, Maue RN, Roache DR, Blake ES, Paxton CH, Mehta CA (2015) The record-breaking 2015 hurricane season in the eastern North Pacific: An analysis of environmental conditions. Geophys Res Lett 43:9217–9224

Dee DP, Uppala SM, Simmons AJ, Berrisford P, Poli P, Kobayashi S, Andrae U, Balmaseda MA, Balsamo G, Bauer P, Bechtold P, Beljaars ACM, van de Berg L, Bidlot J, Bormann N, Delsol C, Dragani R, Fuentes M, Geer AJ, Haimberger L, Healy SB, Hersbach H, Hólm EV, Isaksen L, Kållberg P, Köhler M, Matricardi

M, McNally AP, Monge-Sanz BM, Morcrette JJ, Park BK, Peubey C, de Ros-
nay P, Tavolato C, Thépaut JN, Vitart F (2011) The ERA-Interim reanalysis:
configuration and performance of the data assimilation system. Quart J Roy
Meteor Soc 137:553–597

Di Lorenzo E, Mantua N (2016) Multi-year persistence of the 2014/15 North Pa-
cific marine heatwave. Nature Clim Change 6:1042–1047

Dommenget D, Yu Y (2016) The seasonally changing cloud feedbacks contribution
to the ENSO seasonal phase-locking. Clim Dyn 47:3661–3672

Du Y, Qu T, Meyers G, Masumoto Y, Sasaki H (2005) Seasonal heat budget in
the mixed layer of the southeastern tropical Indian Ocean in a high-resolution
ocean general circulation model. J Geophys Res Oceans 110:C04,012

Fedorov A, Brown JN (2009) Equatorial waves. Encyclopedia of Ocean Sciences,
pp. 3679-3695, Academic, San Diego, Calif.

Hu S, Fedorov AV (2016) Exceptionally strong easterly wind burst stalling El Niño
of 2014. Proceedings of the National Academy of Sciences 113:2005–2010

Hu S, Fedorov AV (2017) The extreme el niño of 2015–2016: the role of westerly
and easterly wind bursts, and preconditioning by the failed 2014 event. Clim
Dyn

Hua LJ, Yu YQ (2015) How are El Niño and La Niña events improves in an eddy-
resolving ocean general circulation model? Atmospheric and Oceanic Science
Letters 8:245

Huang B, Xue Y, Zhang D, Kumar A, McPhaden MJ (2010) The NCEP GODAS
Ocean Analysis of the Tropical Pacific Mixed Layer Heat Budget on Seasonal
to Interannual Time Scales. J Climate 23:4901–4925

Imada Y, Kimoto M (2012) Parameterization of Tropical Instability Waves and Examination of Their Impact on ENSO Characteristics. J Climate 25:4568–4581

Imada Y, Tatebe H, Watanabe M, Ishii M, Kimoto M (2016) South Pacific influence on the termination of El Niño in 2014. Scientific Reports 6

Ishii M, Shouji A, Sugimoto S, Matsumoto T (2005) Objective analyses of sea-surface temperature and marine meteorological variables for the 20th century using ICOADS and the Kobe Collection. Int J Climatol 25:865–879

Jin FF (1997) An equatorial ocean recharge paradigm for ENSO. Part I: Conceptual model. J Atmos Sci 54:811–829

Kalnay E, Kanamitsu M, Kistler R, Collins W, Deaven D, Gandin L, Iredell M, Saha S, White G, Woollen J, Zhu Y, Leetmaa A, Reynolds R, Chelliah M, Ebisuzaki W, Higgins W, Janowiak J, Mo KC, Ropelewski C, Wang J, Jenne R, Joseph D (1996) The NCEP/NCAR 40-Year Reanalysis Project. Bull Amer Meteor Soc 77:437–471

Kanamitsu M, Ebisuzaki W, Woollen J, Yang SK, Hnilo JJ, Fiorino M, Potter GL (2002) NCEP-DOE AMIP-II Reanalysis (R-2). Bull Amer Meteor Soc 83:1631–1643

Kessler WS (1991) Can Reflected Extra-equatorial Rossby Waves Drive ENSO? J Phys Oceanogr 21:444–452

Kessler WS (2002) Is ENSO a cycle or a series of events? Geophys Res Lett 29:2125

Latif M, Biercamp J, von Storch H (1988) The response of a coupled ocean-atmosphere general circulation model to wind bursts. J Atmos Sci 45:964–979

Lengaigne M, Guilyardi E, Boulanger JP, Menkes C, Delecluse P, Inness P, Cole J, Slingo J (2004) Triggering of El Niño by westerly wind events in a coupled general circulation model. Clim Dyn 23:601–620

Levine AFZ, McPhaden MJ (2016) How the July 2014 easterly wind burst gave the 2015–2016 El Niño a head start. Geophys Res Lett 43:6503–6510

L'Heureux ML, Takahashi K, Watkins AB, Barnston AG, Becker EJ, Liberto TED, Gamble F, Gottschalck J, Halpert MS, Huang B, Mosquera-Vázquez K, Wittenberg AT (2016) Observing and Predicting the 2015–16 El Niño. Bull Amer Meteor Soc 0:null

Lorbacher K, Dommenget D, Niiler PP, Kohl A (2006) Ocean mixed layer depth: A subsurface proxy of ocean-atmosphere variability. J Geophys Res Oceans 111:C07,010

Ludescher J, Gozolchiani A, Bogachev MI, Bunde A, Havlin S, Schellnhuber HJ (2014) Very early warning of next El Niño. Proceedings of the National Academy of Sciences 111:2064–2066

McGregor S, Gupta AS, England MH (2012a) Constraining wind stress products with sea surface height observations and implications for pacific ocean sea level trend attribution. J Climate 25:8164–8176

McGregor S, Timmermann A, Schneider N, Stuecker MF, England MH (2012b) The effect of the South Pacific Convergence Zone on the termination of El Niño events and the meridional asymmetry of ENSO. J Climate 25:5566–5586

McGregor S, Timmermann A, Jin FF, Kessler WS (2016) Charging El Niño with off-equatorial westerly wind events. Clim Dyn 47:1111–1125

McPhaden MJ (1999) Genesis and evolution of the 1997-98 El Niño. Science 283:950–954

McPhaden MJ (2015) Playing hide and seek with El Niño. Nature Clim Change 5:791–795

Meinen CS, McPhaden MJ (2000) Observations of warm water volume changes in the equatorial Pacific and their relationship to El Niño and La Niña. J Climate 13:3551–3559

Menkes CE, Lengaigne M, Vialard J, Puy M, Marchesiello P, Cravatte S, Cambon G (2014) About the role of westerly wind events in the possible development of an El Niño in 2014. Geophys Res Lett 41:6476–6483

Moum JN, Perlin A, Nash JD, McPhaden MJ (2013) Seasonal sea surface cooling in the equatorial pacific cold tongue controlled by ocean mixing. Nature 500:64–67

Murakami H, Vecchi GA, Delworth TL, Wittenberg AT, Underwood S, Gudgel R, Yang X, Jia L, Zeng F, Paffendorf K, Zhang W (2017) Dominant Role of Subtropical Pacific Warming in Extreme Eastern Pacific Hurricane Seasons: 2015 and the Future. J Climate 30:243–264

Paek H, Yu JY, Qian C (2017) Why were the 2015/2016 and 1997/1998 extreme el Niños different? Geophys Res Lett 44:1848–1856

Paulson CA, Simpson JJ (1977) Irradiance Measurements in the Upper Ocean. J Phys Oceanogr 7:952–956

Philander SG (1990) El Niño, La Niña, and the Southern Oscillation. Academic Press

Philander SG, Fedorov A (2003) Is El Niño sporadic or cyclic? Annual Review of Earth and Planetary Sciences 31:579–594

Qiu B (2000) Interannual Variability of the Kuroshio Extension System and Its Impact on the Wintertime SST Field. J Phys Oceanogr 30:1486–1502

Qu T (2003) Mixed layer heat balance in the western North Pacific. J Geophys Res Oceans 108:3242

Rasmusson E, Carpenter T (1982) Variations in tropical sea surface temperature and surface wind fields associated with the Southern Oscillation/El Niño. Mon Wea Rev 110:353–384

Rasmusson EM, Arkin PA (1985) Interannual climate variability associated with the El Niño - Southern Oscillation, Elsevier Oceanography Series, vol 40. Elsevier

Rayner NA, Parker DE, Horton EB, Folland CK, Alexander LV, Rowell DP, Kent EC, Kaplan A (2003) Global analyses of sea surface temperature, sea ice, and night marine air temperature since the late nineteenth century. J Geophys Res Atmospheres 108:4407

Santoso A, Gupta AS, England MH (2010) Genesis of Indian Ocean Mixed Layer Temperature Anomalies: A Heat Budget Analysis. J Climate 23:5375–5403

Smith TM, Reynolds RW, Peterson TC, Lawrimore J (2008) Improvements to NOAA's Historical Merged Land-Ocean Surface Temperature Analysis (1880-2006). J Climate 21:2283–2296

Su J, Zhang R, Li T, Rong X, Kug JS, Hong CC (2010) Causes of the El Niño and La Niña Amplitude Asymmetry in the Equatorial Eastern Pacific. J Climate 23:605–617

Thual S, Dewitte B, An S, Ayoub N (2011) Sensitivity of ENSO to Stratification in a Recharge-Discharge Conceptual Model. J Climate 24:4332–4349

Tollefson J (2014) El Niño test forecasters. Nature 508:20–21

Uppala SM, KÅllberg PW, Simmons AJ, Andrae U, Bechtold VDC, Fiorino M, Gibson JK, Haseler J, Hernandez A, Kelly GA, Li X, Onogi K, Saarinen S, Sokka N, Allan RP, Andersson E, Arpe K, Balmaseda MA, Beljaars ACM, Berg LVD, Bidlot J, Bormann N, Caires S, Chevallier F, Dethof A, Dragosavac M, Fisher

M, Fuentes M, Hagemann S, Hólm E, Hoskins BJ, Isaksen L, Janssen PAEM, Jenne R, Mcnally AP, Mahfouf JF, Morcrette JJ, Rayner NA, Saunders RW, Simon P, Sterl A, Trenberth KE, Untch A, Vasiljevic D, Viterbo P, Woollen J (2005) The ERA-40 re-analysis. Quart J Roy Meteorol Soc 131:2961–3012

Vialard J, Menkes C, Boulanger J, Delecluse P, Guilyardi E, McPhaden M, Madec G (2001) A Model Study of Oceanic Mechanisms Affecting Equatorial Pacific Sea Surface Temperature during the 1997–98 El Niño. J Phys Oceanogr 31:1649–1675

Wang W, McPhaden MJ (1999) The surface layer heat balance in the equatorial Pacific Ocean. Part I: Mean seasonal cycle. J Phys Oceanogr 29:1812–1831

Wang W, McPhaden MJ (2000) The surface-layer heat balance in the equatorial Pacific Ocean. Part II: Interannual variability. J Phys Oceanogr 30:2989–3008

Wang W, McPhaden MJ (2001) Surface Layer Temperature Balance in the Equatorial Pacific during the 1997-98 El Niño and 1998-99 La Niña. J Climate 14:3393–3407

Wyrtki K (1985) Water displacements in the Pacific and the genesis of El Niño cycles. J Geophys Res 90:7129–7132

Wyrtki K, Meyers G (1976) The trade wind field over the Pacific Ocean. J Appl Meteor 15:698–704

Xue Y, Kumar A (2017) Evolution of the 2015/16 El Niño and historical perspective since 1979. Science China Earth Sciences 60:1572–1588

Yin Y, Alves O, Oke PR (2011) An Ensemble Ocean Data Assimilation System for Seasonal Prediction. Mon Wea Rev 139:786–808

Zavala-Garay J, Moore AM, Kleeman R (2004) Influence of stochastic forcing on ENSO prediction. J Geophys Res 109:C1107

Zebiak SE, Cane MA (1987) A model of El Niño-Southern Oscillation. Mon Wea Rev 115:2262–2278

"Zhang R, Gao C (2017) Processes involved in the second-year warming of the 2015 el niño event as derived from an intermediate ocean model. Science China Earth Sciences 60:1601–1613

Zhang RH, Endoh M (1994) Simulation of the 1986-1987 El Niño and 1988 La Niña events with a free surface tropical Pacific Ocean general circulation model. J Geophys Res Oceans 99:7743–7759

Table 1 Basin-wide average zonal wind anomalies and their standard deviations in the Northern Hemisphere (Eq.-20°N) and the Southern Hemisphere (20°S-Eq.) and the asymmetry index defined in Sect. 3.1 averaged over 12-month and 24-month periods prior to the event peaks. Units are expressed in $\times\ 10^{-2}$ N m^{-2}. Datasets: GODAS, ERA-Interim and PEODAS.

	-12 months			-24 months		
	2015–16	**1997–98**	**1982–83**	**2015–16**	**1997–98**	**1982–83**
Northern Hemisphere	0.35±0.36	0.64±0.19	0.29±0.08	0.39±0.19	0.46±0.09	0.17±0.08
Southern Hemisphere	-0.53±0.36	0.45±0.04	0.44±0.19	-0.49±0.16	0.16±0.02	0.30±0.13
Asymmetry index	0.85±0.03	0.17±0.17	-0.16±0.15	0.86±0.04	0.29±0.07	-0.13±0.05

Table 2 Projections coefficient values of Kelvin and Rossby waves (see Fig. 6) averaged over 12- and 24-month periods prior to the even peaks and their standard deviations. Units are expressed in m. Dataset: GODAS, ERA-Interim and PEODAS.

		-12 months			-24 months		
		2015−16	**1997−98**	**1982−83**	**2015−16**	**1997−98**	**1982−83**
Kelvin wave		2.6±4.1	14.4±1.7	12.0±1.9	1.4±2.1	7.7±0.6	5.2±1.5
Rossby waves	N = 1	-14.5±3.1	-14.6±1.1	-2.7±5.5	-8.9±1.2	-1.8±1.6	2.2±3.1
	N = 2	-14.4±2.8	-7.1±1.4	-8.9±0.4	-9.4±2.3	-3.3±0.4	-6.2±0.5
	N = 3	-10.8±1.7	-7.4±1.8	-0.9±5.9	-6.6±2.0	-2.3±1.8	2.4±4.5
	N = 4	-13.8±2.7	-0.2±1.5	-3.6±4.1	-11.4±1.3	-1.1±1.3	-1.0±2.1
	N = 5	-4.6±2.4	-5.1±1.9	3.8±7.0	-2.6±1.7	-2.4±2.0	5.5±5.0
	N = 6	-4.7±2.5	-1.5±2.4	-1.7±4.9	-4.2±1.1	-1.9±1.6	0.4±3.1

Table 3 Basin-wide average SSH anomalies in the north-off equatorial region (5°N-15°N) and the equatorial region (5°S-5°N) over 12-month and 24-month periods prior to the event peaks and their standard deviations. Units are expressed in cm. Dataset: GODAS, PEODAS, ORA-S4 and AVISO.

	-12 months			-24 months		
	2015−16	**1997−98**	**1982−83**	**2015−16**	**1997−98**	**1982−83**
North-off Equator	-4.95±0.54	-4.58±0.98	-1.66±0.31	-3.78±0.46	-2.63±0.96	0.15±0.33
Equator	4.67±1.29	5.63±0.51	4.28±0.67	3.28±0.88	2.77±0.09	2.41±0.48
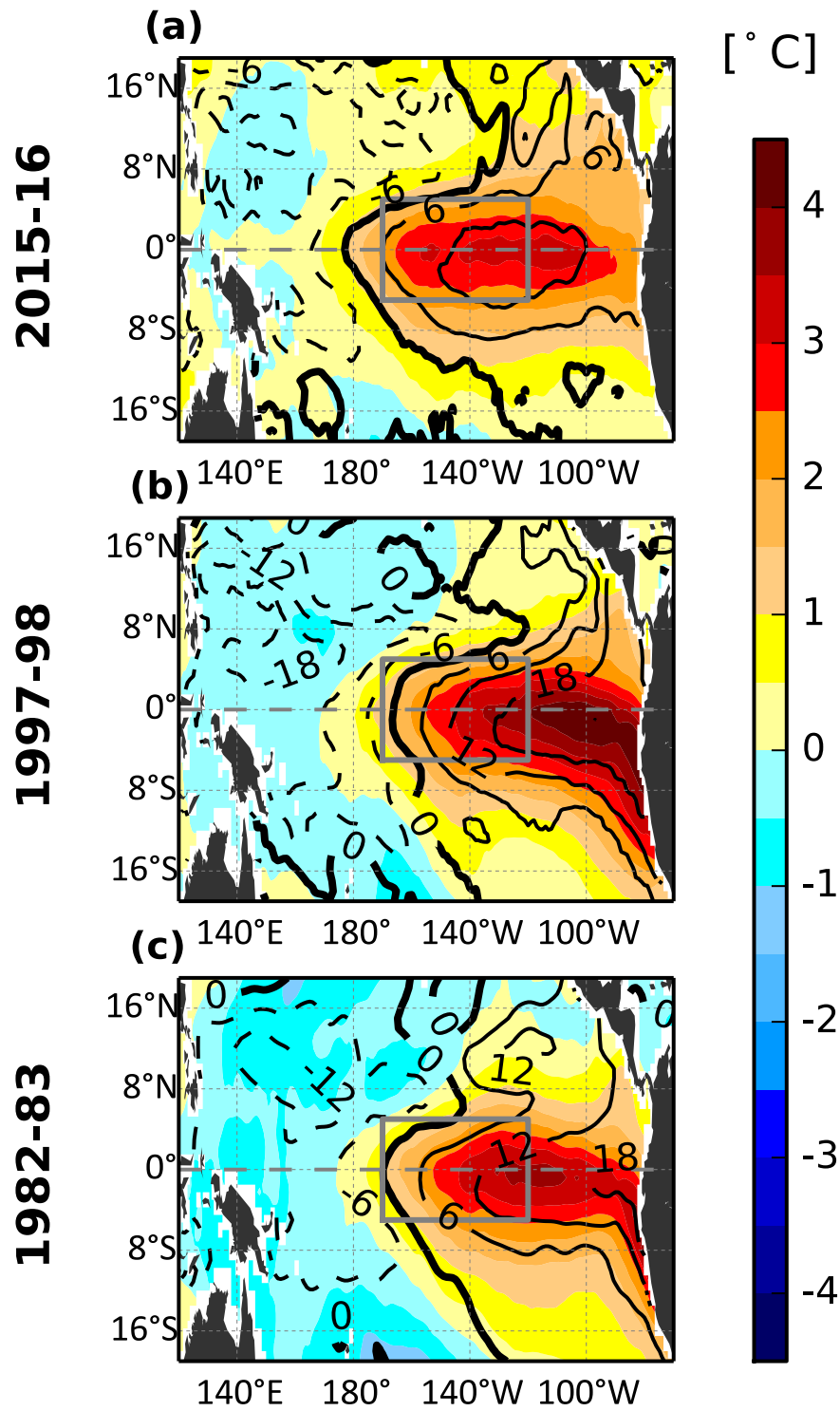
Fig. 1 SST anomalies (shading) and SSH anomalies (contours) in NDJ during the 2015–16 (a), 1997–98 (b) and 1982–83 (c) El Niño events. Note that the contour interval is 6 cm, labels are in cm units and solid contours indicate positive values, bold line zero SSH anomaly, while dashed contours indicate negative values.The dashed gray line indicates the equator and the solid gray box represents the Niño-3.4 region. Datasets for SST: ERSST, HadISST, COBE, ERA-Interim. Datasets for SSH: GODAS, AVISO, PEODAS, ORA-S4.
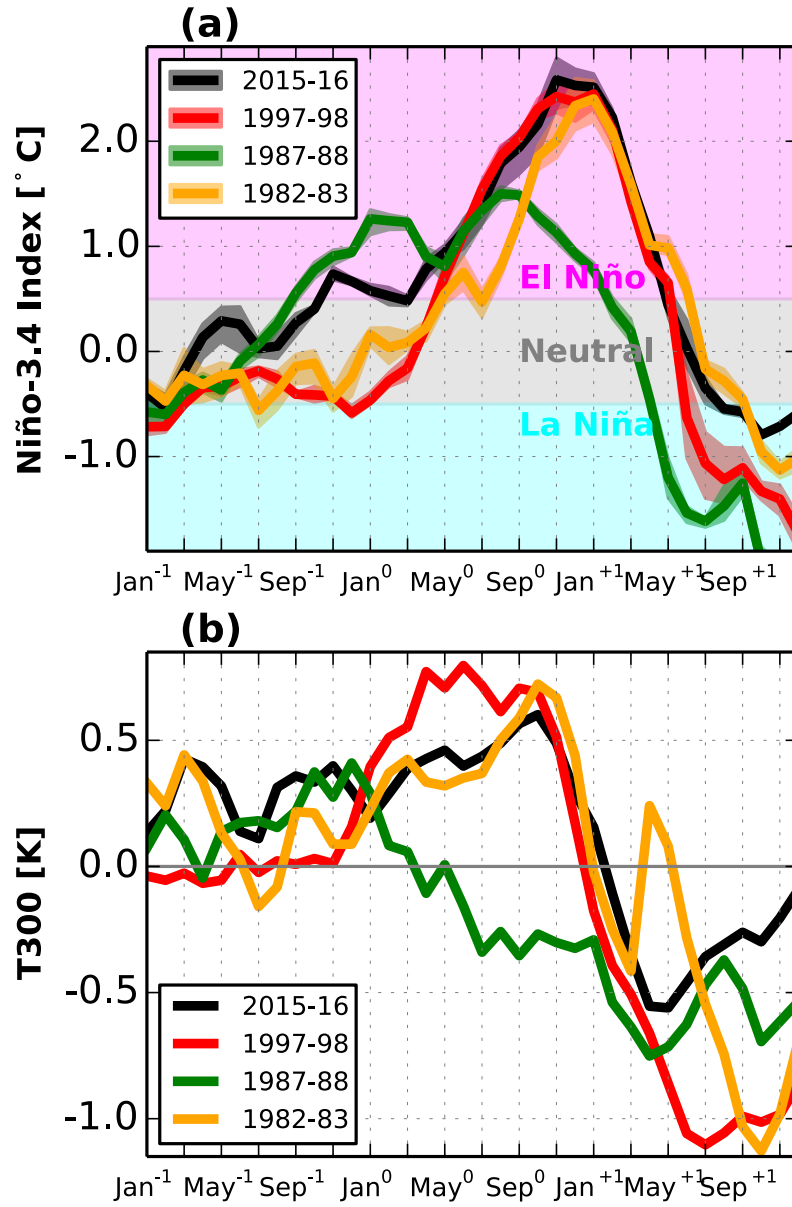
Fig. 2 (a) Sea surface temperature anomalies in the Niño-3.4 region during the two years prior to the peak of strong El Niño event and one year afterward. Solid lines represent mean values of ERSST, HadISST, COBE and ERA-Interim whereas shaded areas represent the one standard deviation envelope of the observed SST. Note that shades in different colors have been used to indicate the three ENSO states. (b) Upper ocean heat content defined as depth averaged temperature in the upper 300 m (GODAS) over the region 5°S-5°N, 120°E-80°W, during the same period as (a).
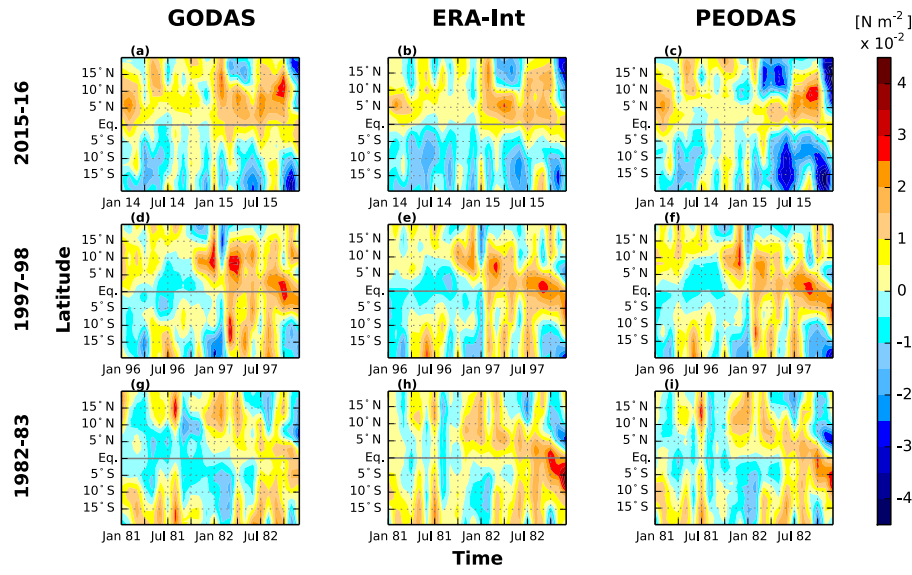
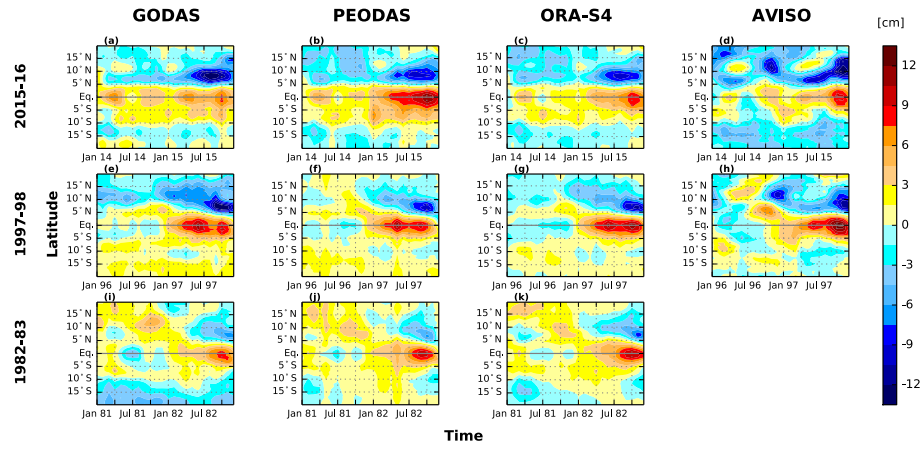**Fig. 3** Zonal wind stress anomalies averaged over 120°E-80°W during the 2-yr period prior to the peak of the (a-c) 2015–16, (d-f) 1997–98, and (g-i) 1982–83 events. Note that gray horizontal lines indicate the equator. Datasets: GODAS, ERA-Interim and PEODAS.
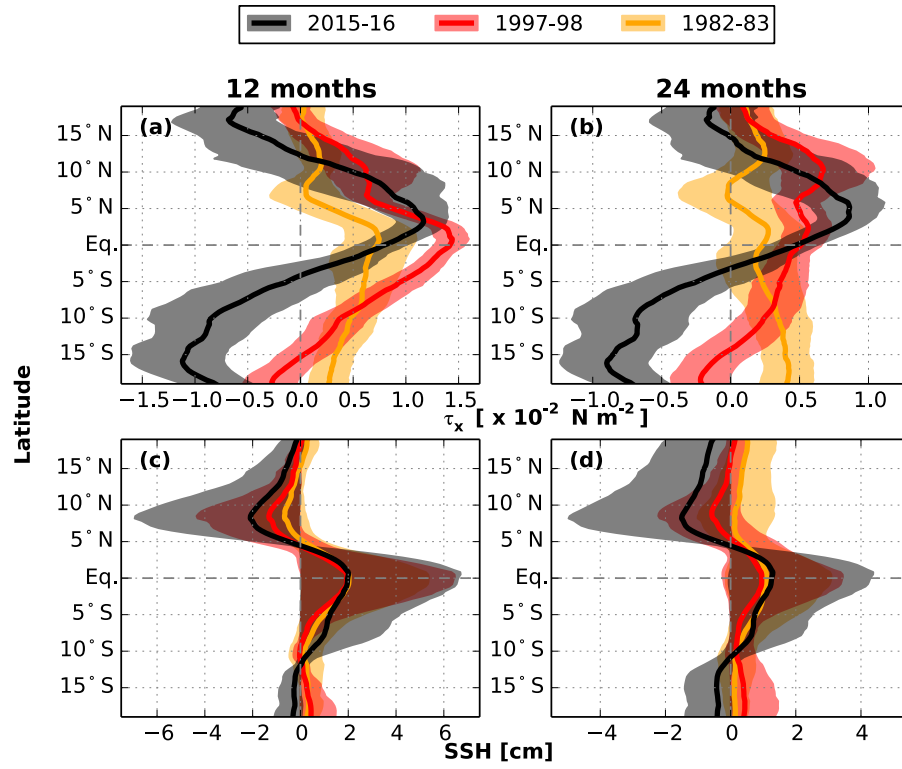
Fig. 4 Zonal wind stress (a,b) and sea surface height (c,d) anomalies averaged over 120°E-80°W and during two periods (12 and 24 months prior to the peak of the events). Solid lines represent the mean values across the datasets: GODAS, PEODAS and ERA-Interim for τ_x; and GODAS, AVISO, PEODAS and ORA-S4 for SSH. The shaded areas show the 5th and 95th percentiles for every monthly value across all products.
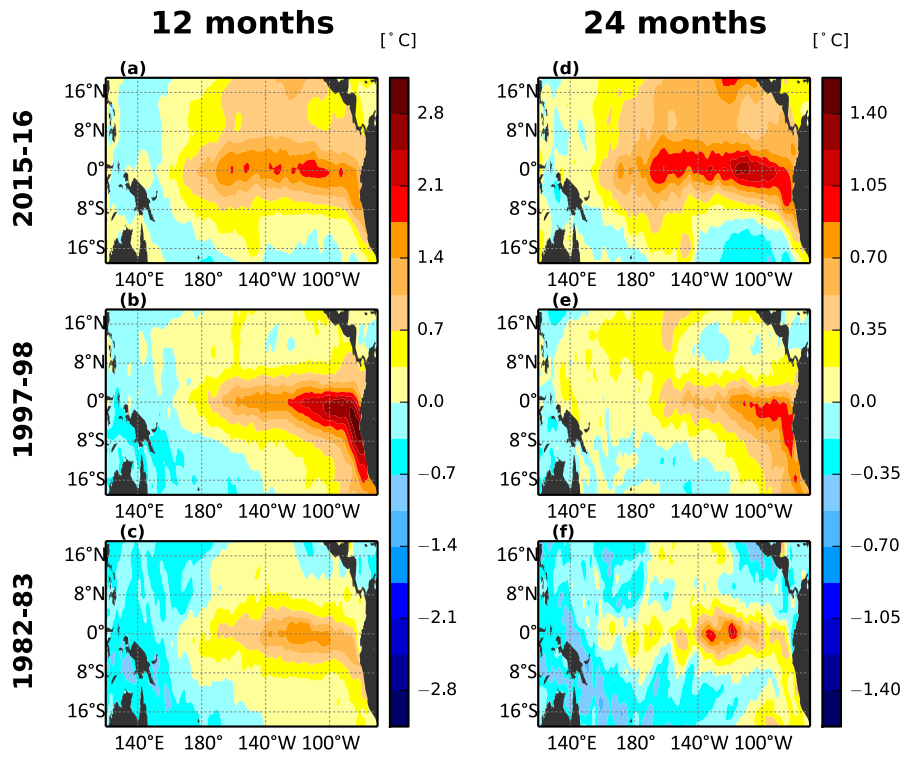
Fig. 5 SST anomalies averaged over the 12-month (a-c) and 24-month (d-f) periods prior to the peak of the 2015–16 El Niño (a, d), 1997–98 El Niño (b, e), and 1982–83 El Niño (c, f) events. Data obtained from HadISST.
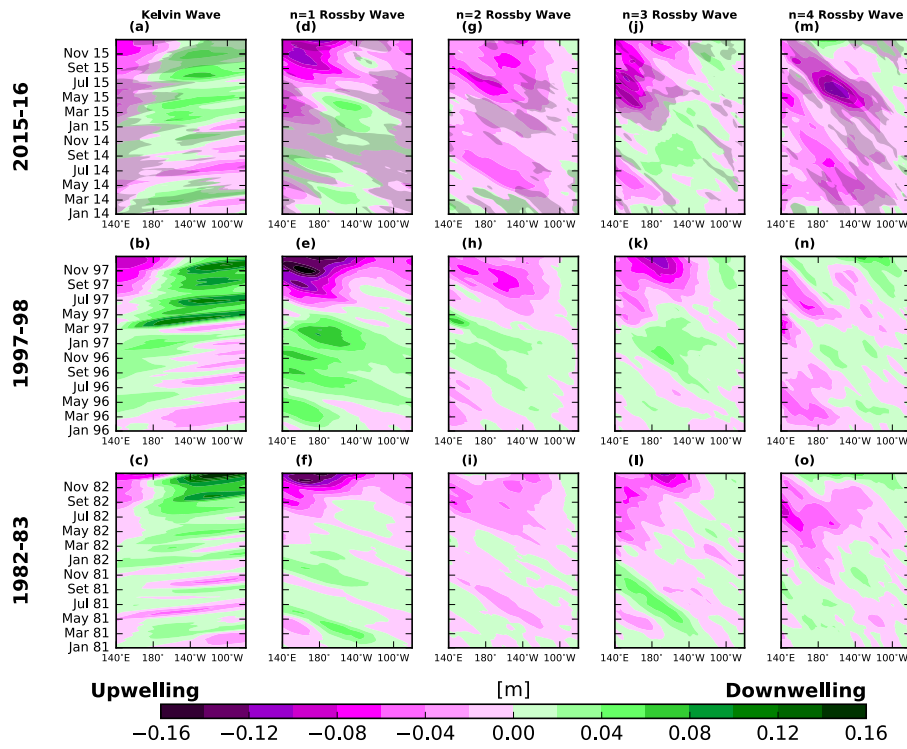
Fig. 6 Hovmöller diagrams of daily projection coefficients across the tropical Pacific Ocean for the (a-c) equatorial Kelvin wave and (d-o) the first four Rossby waves during the 2-yr period prior to the peak of the (first row) 2015–16, (second row) 1997–98, and (third row) 1982–83 events. Wind stress forcing data are obtained from ERA-Interim. Note that gray shadings in the most recent event panels indicate significant difference (calculated from the 3 data sets described in the manuscript) between this event and the 1997–98 and 1982–83 events.

Fig. 7 Sea surface height anomalies averaged over 120°E-80°W during the 2-yr period prior to the peak of the (a-d) 2015–16, (e-h) 1997–98, and (i-k) 1982–83 events. Note that gray horizontal lines indicate the equator. Data are obtained from reanalysis (GODAS, PEODAS and ORA-S4) and observations (AVISO).
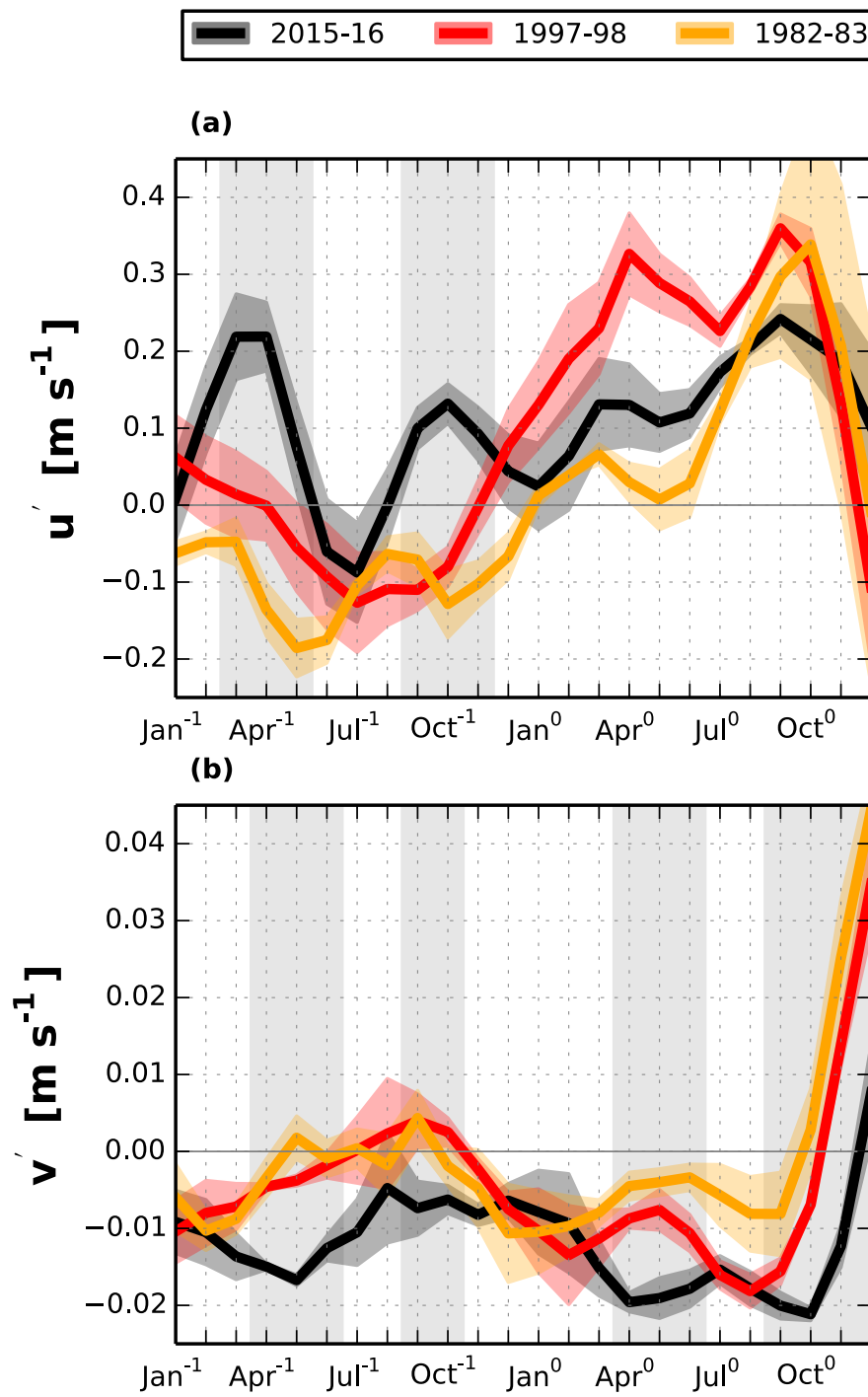
Fig. 8 Time series of zonal (a) and meridional (b) ocean currents averaged over the Niño-3.4 region and integrated vertically over the mixed layer. The gray shading indicates that the 2015–16 El Niño values are significantly different to the other two events. Datasets: GODAS, PEODAS, ORA-S4.
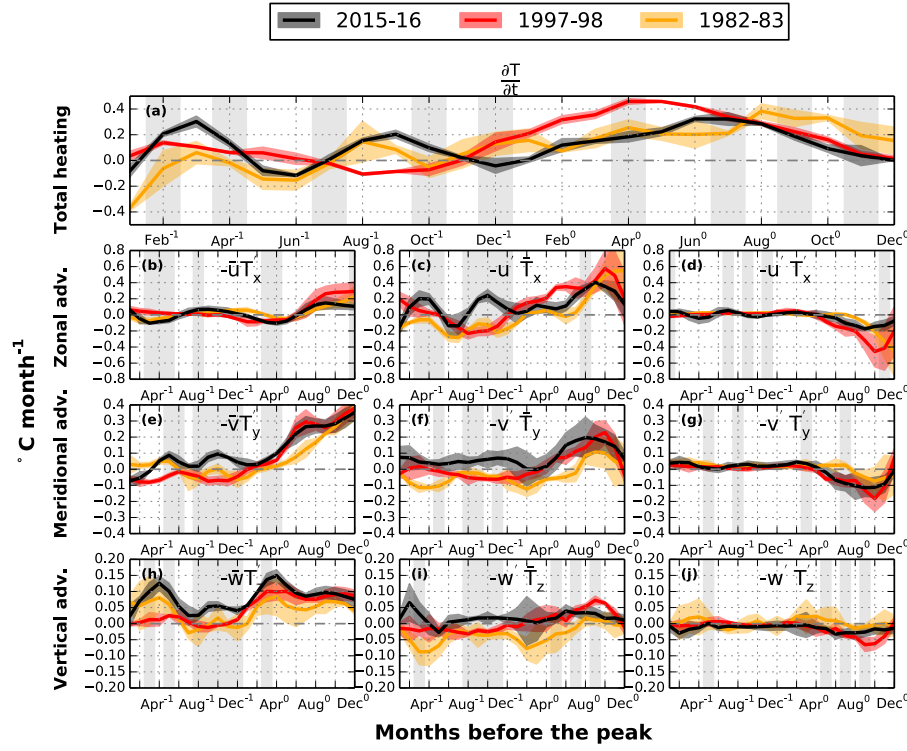
Fig. 9 The time evolution of temperature budget anomalies of the strong El Niño events in the Niño-3.4 region for the total heating (a), zonal (b-d), meridional (e-g), and vertical (h-j) advection terms of the heat budget equation. A three-month running average is calculated. The events are averaged across the three datasets (GODAS, PEODAS and ORA-S4) and shown their standard deviation (shading). The gray shading indicates that the 2015–16 El Niño values are significantly different to the other two events. Different y-axis heating scales are employed in each direction of advective terms.
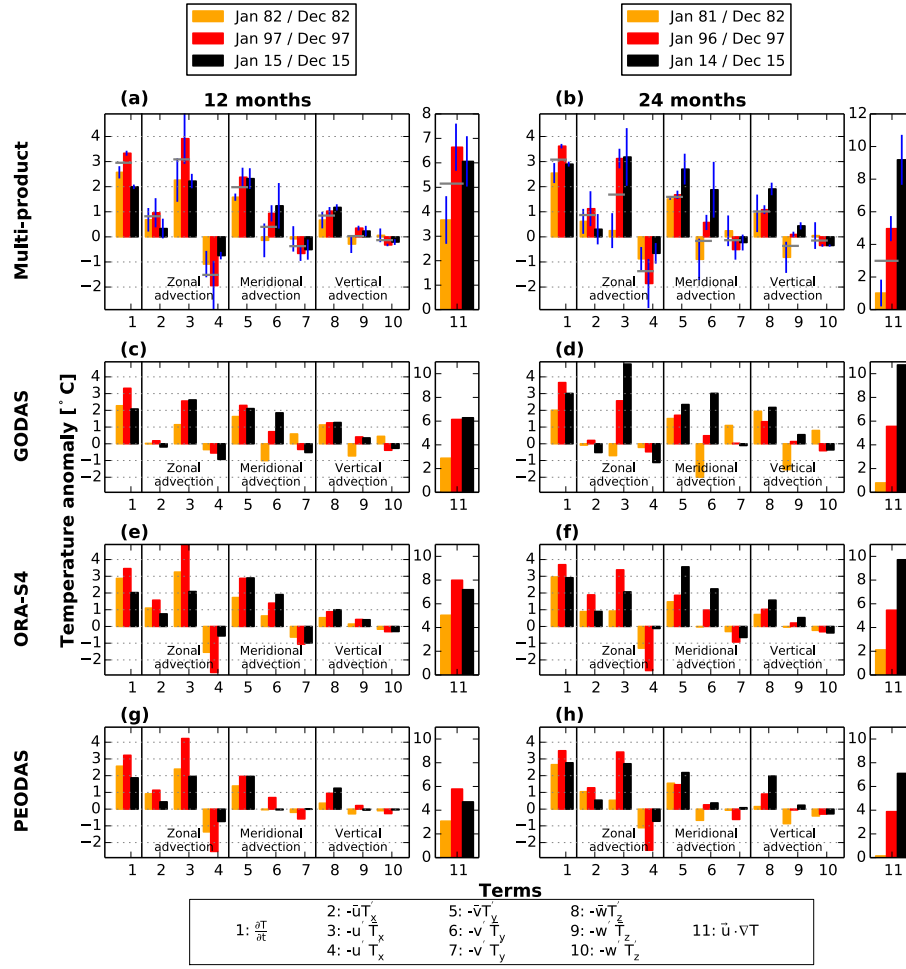
Fig. 10 Contribution of each individual advection term of the heat budget equation and the total advective term integrated over (left column) 12 and (right column) 24 months before the peak, and averaged over the Niño-3.4 region, for all datasets (a, b), GODAS (c, d), ORA-S4 (e, f) and PEODAS (g, h). Orange, red and black shaded vertical bars represent the 1982–83, the 1997–98, and the 2015–16 El Niño events, respectively. The gray horizontal bars in panels (a) and (b) indicate the composite mean for each term across the 1982–83 and 1997–98 events, and the error bars represent the standard deviation across the three datasets for each event.
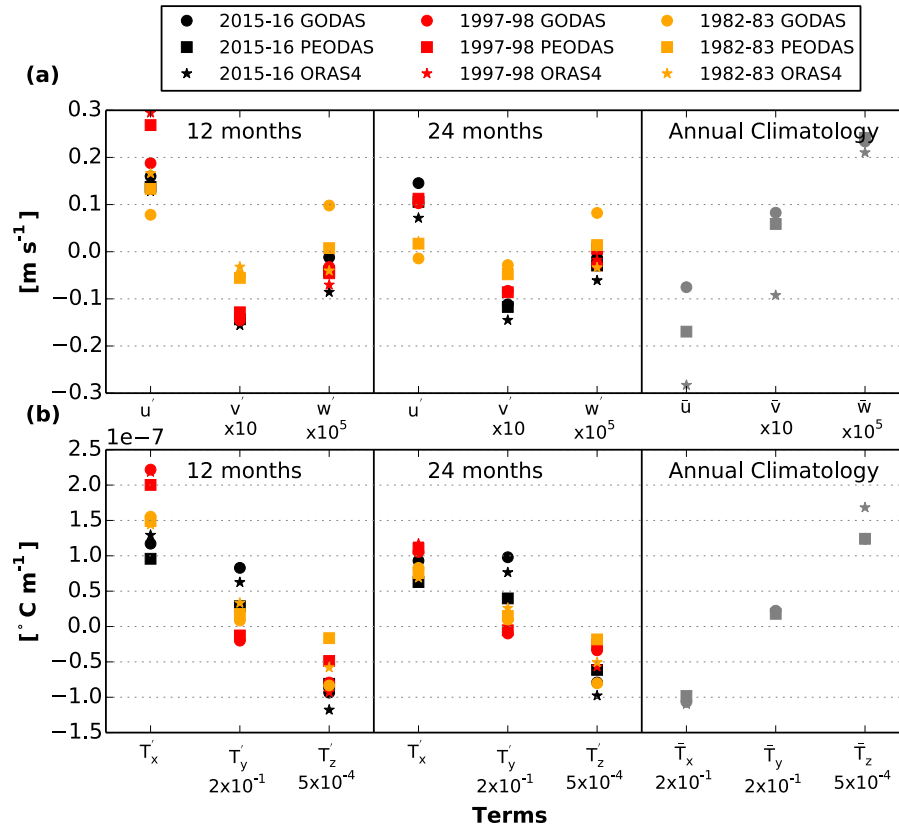
Fig. 11 Averaged values of ocean currents (a) and temperature gradients (b) over the Niño-3.4 region during the 12-month and 24-month periods and annual mean climatology for each reanalysis product and each event. Note the different scale used for some terms.
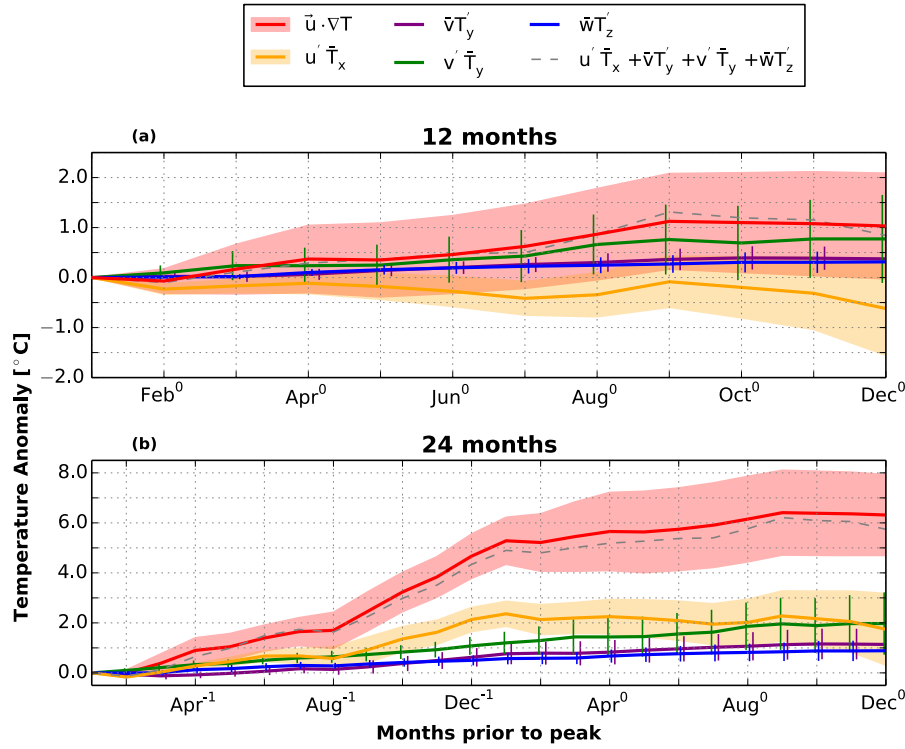
Fig. 12 Temperature anomalies in the Niño-3.4 region integrated over the mixed layer according to all anomalous advective terms and those with statistically significant differences between the events starting from 0 anomaly at the beginning of (a) 12 months and (b) 24 months before the observed peak. Solid lines represent the mean across the three products (GODAS, PEODAS and ORA-S4), vertical lines and shading areas indicate the standard deviation across the three products. Note that these anomalous terms in 2015–16 event are computed as the deviation of the 1997–98 and 1982–83 average.
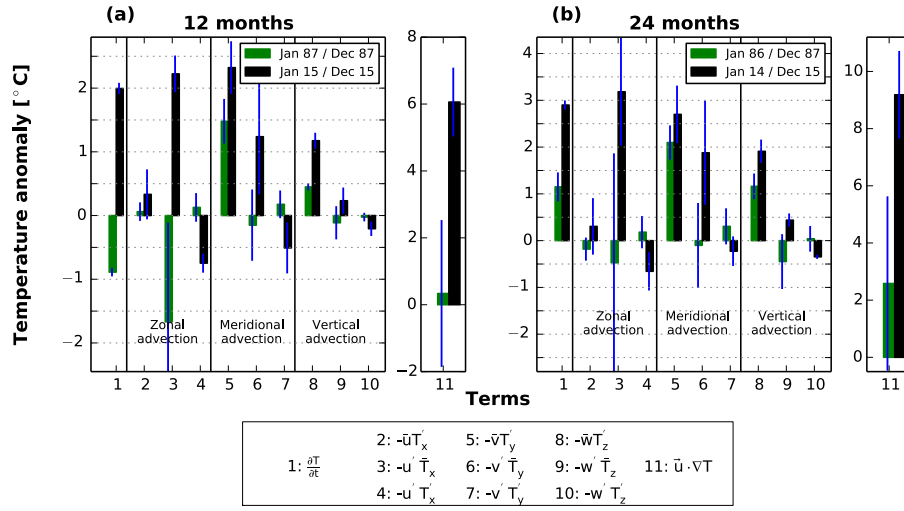
Fig. 13 Contribution of each individual advection term of the heat budget equation and the total advective term integrated over time, summed up over (a) 12 and (b) 24 months before the peak, and averaged over the Niño-3.4 region. Green and black shaded vertical bars represent the 1987–88, and the 2015–16 El Niño events, respectively. The error bars represent the standard deviation across the three datasets. Datasets: GODAS, PEODAS, ORA-S4.
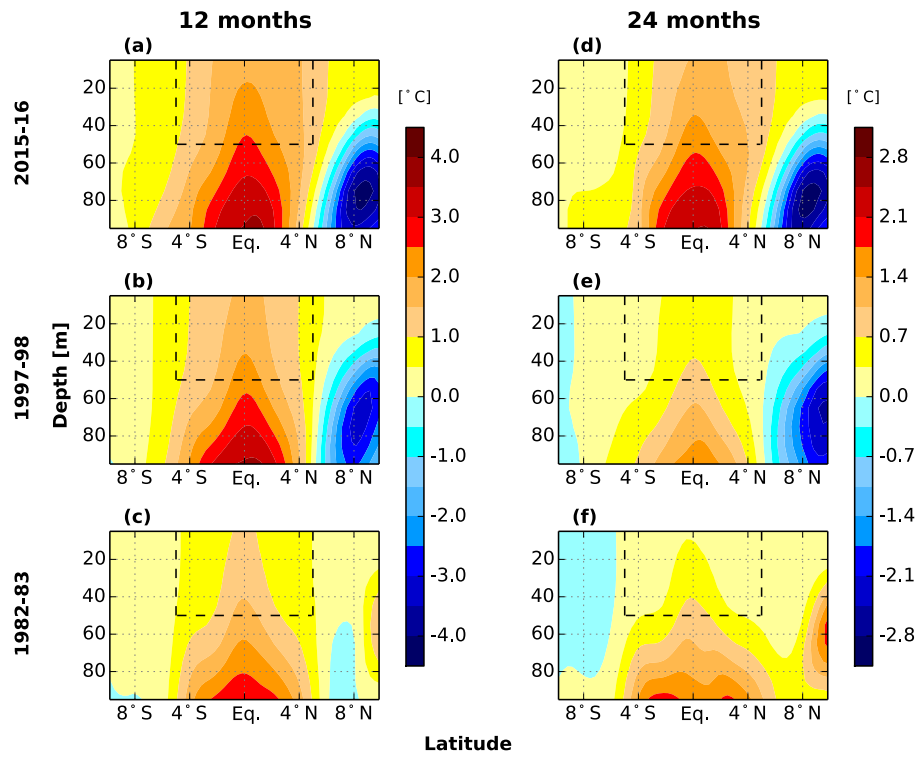
Fig. 14 Vertical profile of anomalous potential temperature averaged over the Niño-3.4 region across latitude during both the 12-month (a–c) and 24-month (d–f) periods prior to the peak of the events. Note that black dashed lines represent the meridional (5°S-5°N) and vertical (50 m) domain considered in this study. Dataset: GODAS.
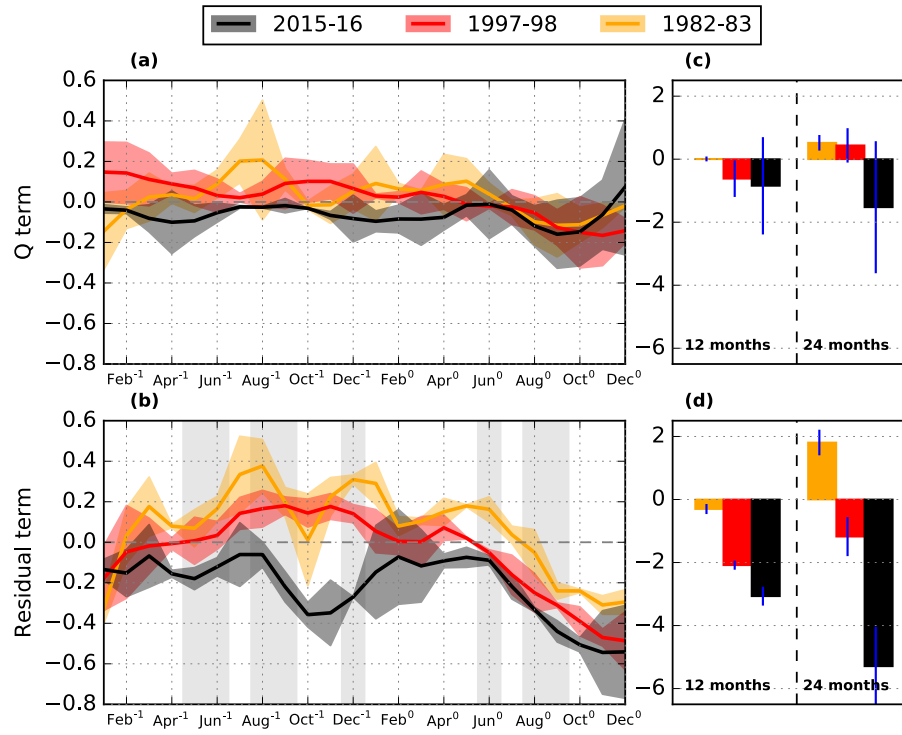
Fig. 15 (a–b) As in Fig. 10, the time evolution of temperature budget anomalies in the Niño-3.4 region for the total heat flux and residual terms, respectively. (c–d) Contribution of the total heat flux and residual terms of the heat budget equation over 12 and 24 months before the peak, and averaged over the Niño-3.4 region. Note that Q_{net} is not available for ORA-S4.